Progress In Electromagnetics Research B, Vol. 20, 65–90, 2010

RECONSTRUCTION AND VISUALIZATION OF EQUIVALENT CURRENTS ON A RADOME USING AN INTEGRAL REPRESENTATION FORMULATION

K. Persson, M. Gustafsson, and G. Kristensson

Department of Electrical and Information Technology
Electromagnetic Theory
Lund University
Box 118, Lund SE-22100, Sweden

Abstract—In this paper an inverse source problem is investigated. The measurement set-up is a reflector antenna covered by a radome. Equivalent currents are reconstructed on a surface shaped as the radome in order to diagnose the radome's interaction with the radiated field. To tackle this inverse source problem an analysis of a full-wave integral representation, with the equivalent currents as unknowns, is used. The extinction theorem and its associated integral equation ensure that the reconstructed currents represent sources within the radome. The axially symmetric experimental set-up reduces the computational complexity of the problem. The resulting linear system is inverted by using a singular value decomposition. We visualize how the presence of the radome alters the components of the equivalent currents. The method enables us to determine the phase shift of the field due to the transmission of the radome, i.e., the IPD (insertion phase delay). Also, disturbances due to defects, not observable in the measured near field, are localized in the equivalent currents.

1. INTRODUCTION

The aim of this paper is to calculate and visualize the sources of a measured electric field on a radome-shaped surface. The electric field is originating from an antenna inside the radome and is measured in the near-field zone outside the radome. The electrical size of the radome is 29 wavelengths at the frequency 8.0 GHz.

This kind of calculations are important in diagnosing antennas, designing radomes, etc, since the field close to the body of interest

---

Corresponding author: K. Persson (kristin.persson@eit.lth.se).

is difficult to measure directly. By doing so, the interaction between the source and the measurement probe can give incorrect results [1–3]. In the process of designing a radome, the electric field close to the antenna is input to software calculating the field propagation through the radome wall [4, 5]. To get reliable results, it is crucial that the representation of the field radiated from the antenna, i.e., the input data, is well known. To determine the performance of the radome it is eligible to quantify, e.g., beam deflection, transmission efficiency, pattern distortion, and the electrical thickness of the radome wall, i.e., the insertion phase delay (IPD). It is also of interest to see how the mounting device and, e.g., lightning conductors and Pitot tubes, often placed on radomes, interact with the electric field.

One of the first techniques developed to solve the inverse source problems of this kind employs the plane wave expansion [6–8]. The method works very well when the equivalent currents are reconstructed on a planar surface. One recent area of application is the determination of the specific absorption rate of mobile phones [9]. A modal expansion of the field can be utilized if the reconstruction surface is cylindrical or spherical [1, 10, 11]. This method has been used to calculate the insertion phase delay (IPD) and to detect defects on a spherical radome [12]. More general geometries, e.g., needle shaped objects and flat disks, can be handled by expanding the field in spheroidal wave functions [13]. A combination of the plane wave spectrum and the modal expansion has been utilized in [14–16] where flat antenna structures are diagnosed and safety perimeter of base stations' antennas is investigated, respectively. Further references in the area can be found in [17].

To be able to handle a wider class of geometries, diagnostic techniques based on integral representations, which are solved by a method of moment approach, are applied. The drawback is the computational complexity. If the object on which the currents are to be reconstructed is metallic, i.e., a perfect electric conductor (PEC), either the electric or magnetic field integral equation (EFIE or MFIE) can be employed [18] or combinations thereof [19, 20]. The equivalence principle is conveniently used when analyzing flat antenna structures [21–23]. An integral representation together with *a priori* information of the object and iterative solvers is used by [24, 25] to find the electric current on the walls of a PEC for diagnose of a pyramidal horn antenna and a monopole placed on the chassis of a car. In [26] a dual-surface approach is compared to the single-equation formulation.

In this paper we propose a technique using the integral representations to relate the unknown equivalent currents to a known measured near field. In addition to the integral representation, we also use an integral equation, originating from the extinction theorem [27]. By using the extinction theorem together with the integral representation, we secure that the sources of the reconstructed currents only exist inside the enclosing volume [28]. The equivalent currents can be reconstructed on a surface arbitrarily close to the antenna. No *a priori* information of the material of the object just inside the surface is utilized.

2. PREREQUISITES

In this section, we review the basic equations employed in this paper. We start with a general geometry, and specialize to a body of revolution in Section 2.2. More technical details are given in [29].

2.1. General Case

The surface integral representation expresses the electromagnetic field in a homogeneous, isotropic region in terms of its values on the closed bounding surface. We engage the integral representations to a domain outside a closed, bounded surface S_{rad}. Carefully employing the Silver-Müller radiation conditions, the solution of the Maxwell equations satisfy the following integral representation [28, 30–32]

$$\iint_{S_{\text{rad}}} \Bigg(-\mathrm{j}\omega\mu_0\mu \; g(\mathbf{r}_1,\mathbf{r}_2)\big[\hat{\mathbf{n}}(\mathbf{r}_1)\times\mathbf{H}(\mathbf{r}_1)\big] + \frac{\mathrm{j}}{\omega\epsilon_0\epsilon}\; \nabla_1 g(\mathbf{r}_1,\mathbf{r}_2)\Big\{\nabla_{1S}\cdot\big[\hat{\mathbf{n}}(\mathbf{r}_1)\times\mathbf{H}(\mathbf{r}_1)\big]\Big\} - \nabla_1 g(\mathbf{r}_1,\mathbf{r}_2)\times\big[\hat{\mathbf{n}}(\mathbf{r}_1)\times\mathbf{E}(\mathbf{r}_1)\big]\Bigg)\,\mathrm{d}S_1 = \begin{cases}\mathbf{E}(\mathbf{r}_2) & \mathbf{r}_2 \text{ outside } S_{\text{rad}}\\ \mathbf{0} & \mathbf{r}_2 \text{ inside } S_{\text{rad}}\end{cases} \tag{1}$$

where the time convention used is $\mathrm{e}^{\mathrm{j}\omega t}$, and the surface divergence is denoted $\nabla_S\cdot$ [27]. The variable of integration is denoted $\mathbf{r}_1$ and the observation point $\mathbf{r}_2$, see Figure 1. The relative permittivity ϵ and the relative permeability μ may depend on the angular frequency ω, i.e., the material can be dispersive, but they are constants as functions of space (homogeneous material). The scalar free space Green function is

$$g(\mathbf{r}_1,\mathbf{r}_2) = \frac{\mathrm{e}^{-\mathrm{j}k|\mathbf{r}_2-\mathbf{r}_1|}}{4\pi|\mathbf{r}_2-\mathbf{r}_1|}$$

where the wave number of the material is $k = \omega\sqrt{\epsilon_0\mu_0\epsilon\mu}$. The representation (1) states that if the total electromagnetic field on S_{rad} is known, the total electromagnetic field outside S_{rad} can be

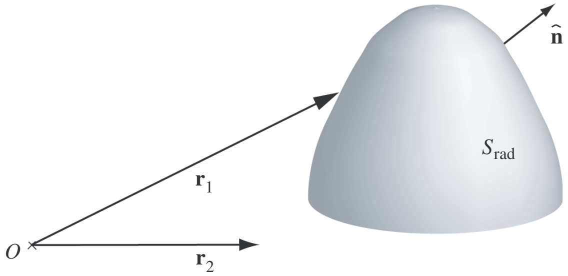

Figure 1. The surface $S_{\rm rad}$ of integration. The unit normal to the surface is $\hat{\mathbf{n}}$. The variable of integration is denoted $\mathbf{r}_1$ and the observation point $\mathbf{r}_2$.

determined [28, 33, 34]. If these integrals are evaluated at a point $\mathbf{r}_2$ lying in the volume enclosed by $S_{\rm rad}$ these integrals cancel each other (extinction). It is important to notice that this does not necessarily mean that the field $\mathbf{E}$ is identically zero inside $S_{\rm rad}$, it only states that the values of the integrals cancel.

The electric and magnetic equivalent surface current densities, $\mathbf{J}$ and $\mathbf{M}$, are introduced to simplify the notation and they are defined as [35]

$$\begin{cases} \mathbf{J}(\mathbf{r}) = \hat{\mathbf{n}}(\mathbf{r}) \times \mathbf{H}(\mathbf{r}) \\ \mathbf{M}(\mathbf{r}) = -\hat{\mathbf{n}}(\mathbf{r}) \times \mathbf{E}(\mathbf{r}) \end{cases} \tag{2}$$

The lower (or upper) representation in (1) is transformed into an integral equation letting $\mathbf{r}_2$ approach $S_{\rm rad}$. However, care must be taken since the integrands become singular when $\mathbf{r}_2$ approaches the surface [27, 28, 31, 36]. The equation consists of three components, two describing the tangential field and one describing the normal component of the field. Since the normal component can be determined by the knowledge of the tangential parts, this representation has redundancies, i.e., the normal component is eliminated [32].

To this end, (1) splits into a surface integral representation of the electric field

$$\iint\limits_{S_{\rm rad}} \Big\{ -\mathrm{j}\omega\mu_0\mu\; g(\mathbf{r}_1,\mathbf{r}_2)\mathbf{J}(\mathbf{r}_1) + \mathrm{j}\frac{1}{\omega\epsilon_0\epsilon}\;\nabla_1 g(\mathbf{r}_1,\mathbf{r}_2)\big[\nabla_{1S}\cdot\mathbf{J}(\mathbf{r}_1)\big] \\ +\nabla_1 g(\mathbf{r}_1,\mathbf{r}_2)\times\mathbf{M}(\mathbf{r}_1)\Big\}\,\mathrm{d}S_1 = \mathbf{E}(\mathbf{r}_2) \qquad \mathbf{r}_2 \text{ outside } S_{\rm rad} \tag{3}$$

and a surface integral equation in $\mathbf{J}$ and $\mathbf{M}$

$$\hat{\mathbf{n}}(\mathbf{r}_2)\times\iint\limits_{S_{\text{rad}}}\Big\{\mathrm{j}\omega\mu_0\mu\; g(\mathbf{r}_1,\mathbf{r}_2)\mathbf{J}(\mathbf{r}_1)-\mathrm{j}\frac{1}{\omega\epsilon_0\epsilon}\;\nabla_1 g(\mathbf{r}_1,\mathbf{r}_2)\big[\nabla_{1S}\cdot\mathbf{J}(\mathbf{r}_1)\big]$$
$$-\nabla_1 g(\mathbf{r}_1,\mathbf{r}_2)\times\mathbf{M}(\mathbf{r}_1)\Big\}\;\mathrm{d}S_1=\frac{1}{2}\mathbf{M}(\mathbf{r}_2)\qquad \mathbf{r}_2\in S_{\text{rad}} \tag{4}$$

When necessary, the integrals in the surface integral equation are interpreted as Cauchy's principal value [27, 37].

The integral equation is written in a weak form, i.e., it is multiplied by a test function, $\boldsymbol{\Psi}$, and integrated over its domain [19, 36, 38, 39]

$$\mathrm{j}\omega\mu_0\mu\iint\limits_{S_{\text{rad}}}\iint\limits_{S_{\text{rad}}}\boldsymbol{\Psi}(\mathbf{r}_2)\cdot g(\mathbf{r}_1,\mathbf{r}_2)\mathbf{J}(\mathbf{r}_1)\;\mathrm{d}S_1\;\mathrm{d}S_2$$
$$-\mathrm{j}\frac{1}{\omega\epsilon_0\epsilon}\iint\limits_{S_{\text{rad}}}\iint\limits_{S_{\text{rad}}}\big[\nabla_{2S}\cdot\boldsymbol{\Psi}(\mathbf{r}_2)\big]g(\mathbf{r}_1,\mathbf{r}_2)\big[\nabla_{1S}\cdot\mathbf{J}(\mathbf{r}_1)\big]\;\mathrm{d}S_1\;\mathrm{d}S_2$$
$$-\iint\limits_{S_{\text{rad}}}\iint\limits_{S_{\text{rad}}}\boldsymbol{\Psi}(\mathbf{r}_2)\cdot\big[\nabla_1 g(\mathbf{r}_1,\mathbf{r}_2)\times\mathbf{M}(\mathbf{r}_1)\big]\;\mathrm{d}S_1\;\mathrm{d}S_2$$
$$-\frac{1}{2}\iint\limits_{S_{\text{rad}}}\big[\hat{\mathbf{n}}(\mathbf{r}_2)\times\boldsymbol{\Psi}(\mathbf{r}_2)\big]\cdot\mathbf{M}(\mathbf{r}_2)\;\mathrm{d}S_2=0 \tag{5}$$

The evaluation of the integrals in this paper is restricted to a body of revolution, see Section 2.2, and follows the scheme in [40, 41].

2.2. Body of Revolution

From now on the equations are adapted to a body of revolution (BOR) in vacuum, i.e., $\epsilon = 1$ and $\mu = 1$. The surface is parameterized by the azimuth angle φ and the height coordinate along the surface v, i.e., the position vector $\mathbf{r}$ can be expressed as $\mathbf{r}(\varphi, v) = \rho(v)\cos\varphi\,\hat{\mathbf{e}}_{\text{x}} + \rho(v)\sin\varphi\,\hat{\mathbf{e}}_{\text{y}} + z(v)\,\hat{\mathbf{e}}_{\text{z}}$. The normalized basis vectors are then

$$\hat{\boldsymbol{\varphi}}(\varphi)=\frac{\partial\mathbf{r}}{\partial\varphi}\Big/\left|\frac{\partial\mathbf{r}}{\partial\varphi}\right|=-\sin\varphi\,\hat{\mathbf{e}}_{\text{x}}+\cos\varphi\,\hat{\mathbf{e}}_{\text{y}}\quad\text{and}\quad\hat{\mathbf{v}}(\varphi,v)=\frac{\partial\mathbf{r}}{\partial v}\Big/\left|\frac{\partial\mathbf{r}}{\partial v}\right|$$

and $\{\hat{\mathbf{n}}, \hat{\boldsymbol{\varphi}}, \hat{\mathbf{v}}\}$ forms a right-handed triple of unit vectors, see Figure 2. The curvilinear components of the magnetic equivalent surface current and electric field are denoted as $E^{\varphi} = -M^{\text{v}}$ and $E^{\text{v}} = M^{\varphi}$, cf., (2), where $M^{\varphi} = \mathbf{M}\cdot\hat{\boldsymbol{\varphi}}$, and $M^{\text{v}} = \mathbf{M}\cdot\hat{\mathbf{v}}$. The magnetic field and the electric equivalent current are related in a similar way.

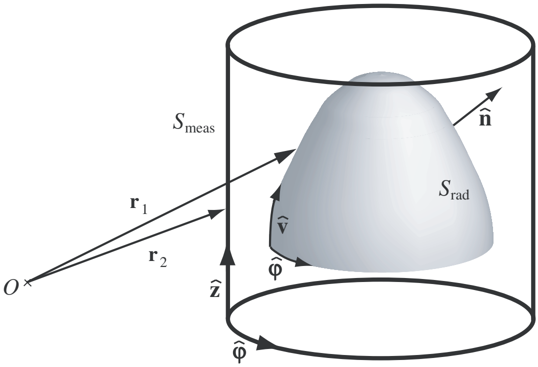

Figure 2. The regions of integration in (8).

Two functions, $\mathbf{a}_{mj}^{\varphi}$ and $\mathbf{a}_{mj}^{\text{v}}$, are used as basis functions. They are defined as

$$\begin{aligned}\mathbf{a}_{mj}^{\varphi} &= f_j^{\varphi}(v)\,\mathrm{e}^{\mathrm{j}m\varphi}\hat{\boldsymbol{\varphi}}\\ \mathbf{a}_{mj}^{\text{v}} &= f_j^{\text{v}}(v)\,\mathrm{e}^{\mathrm{j}m\varphi}\hat{\mathbf{v}}\end{aligned}\tag{6}$$

The height of the radome, v_1, is discretized into points, v_j, where $j = 1, \ldots, N_{\text{z}}$. The functions $f_j^{\varphi/\text{v}}(v)$ can be chosen as a constant, linear, cubic, spline functions etc, with support in a neighborhood of v_j [19, 38]. For the results in this paper, both $f_j^{\varphi/\text{v}}(v)$ are chosen as piecewise linear functions, i.e., one-dimensional rooftops. Observe that φ/v in $f^{\varphi/\text{v}}$ denotes a superscript and not an exponential. In the azimuthal direction, a global function, $\mathrm{e}^{\mathrm{j}m\varphi}$, i.e., a Fourier basis, is used due to the symmetry of the body, and m is an integer index. The magnetic current is expanded as

$$\mathbf{M} = \sum_{m,j}\left\{M_{mj}^{\varphi}\,\mathbf{a}_{mj}^{\varphi} + M_{mj}^{\text{v}}\,\mathbf{a}_{mj}^{\text{v}}\right\}\tag{7}$$

The electric current $\mathbf{J}$ is expanded in a similar way, but with expansion coefficients $J_{mj}^{\varphi/\text{v}}$. Galerkin's method is used [38]. That is, the test functions are according to (6) $\boldsymbol{\Psi}_{ni}^{\varphi} = (\mathbf{a}_{ni}^{\varphi})^*$ and $\boldsymbol{\Psi}_{ni}^{\text{v}} = (\mathbf{a}_{ni}^{\text{v}})^*$ where complex conjugation is denoted by a star and the indicies run through the same integers as m and j.

The surface integral representation in (3) is applied to the measurement set-up described in Section 3, i.e., $\mathbf{r}_2$ belongs to a cylindrical surface S_{meas}, see Figure 2. This surface has axial symmetry with constant radius and is parameterized by φ_2 and v_2, in the same manner as the surface S_{rad} is. The height is discretized into points, v_q, where $q = 1, \ldots, N_{\text{z}}^{\text{meas}}$. None of the integrals contains singularities since $\mathbf{r}_1$ and $\mathbf{r}_2$ will not coincide. From Equation (3), we get

$$\begin{aligned}&\begin{bmatrix}\hat{\mathbf{v}}\\ \hat{\boldsymbol{\varphi}}\end{bmatrix}\cdot\Bigg\{-\mathrm{j}\omega\mu_0\iint\limits_{S_{\mathrm{rad}}} g(\mathbf{r}_1,\mathbf{r}_2)\mathbf{J}(\mathbf{r}_1)\ \mathrm{d}S_1\\ &+\mathrm{j}\frac{1}{\omega\epsilon_0}\iint\limits_{S_{\mathrm{rad}}}\nabla_1 g(\mathbf{r}_1,\mathbf{r}_2)\big[\nabla_{1S}\cdot\mathbf{J}(\mathbf{r}_1)\big]\ \mathrm{d}S_1\\ &+\iint\limits_{S_{\mathrm{rad}}}\nabla_1 g(\mathbf{r}_1,\mathbf{r}_2)\times\mathbf{M}(\mathbf{r}_1)\ \mathrm{d}S_1\Bigg\}=\begin{bmatrix}\hat{\mathbf{v}}\cdot\mathbf{E}(\mathbf{r}_2)\\ \hat{\boldsymbol{\varphi}}\cdot\mathbf{E}(\mathbf{r}_2)\end{bmatrix}=\begin{bmatrix}E^{\mathrm{v}}(\varphi_2,v_2)\\ E^{\varphi}(\varphi_2,v_2)\end{bmatrix}\end{aligned}\tag{8}$$

where $\mathbf{r}_2 \in S_{\mathrm{meas}}$ and the tangential components are projected. The right hand side of (8) is expanded in a Fourier series. The Fourier series reduce the dimensions of the problem by one degree [19, 40, 42].

The representation in (8) and the integral equation in (5) are organized as a system of matrices, i.e.,

$$\begin{bmatrix} Z^{11} & Z^{12}\\ Z^{21} & Z^{22}\end{bmatrix}\begin{bmatrix} J^{\mathrm{v}}\\ J^{\varphi}\end{bmatrix}+\begin{bmatrix} X^{11} & X^{12}\\ X^{21} & X^{22}\end{bmatrix}\begin{bmatrix} M^{\mathrm{v}}\\ M^{\varphi}\end{bmatrix}=\begin{bmatrix} E^{\mathrm{v}}\\ E^{\varphi}\end{bmatrix}\tag{9}$$

and

$$\begin{bmatrix} \mathcal{Z}^{11} & \mathcal{Z}^{12}\\ \mathcal{Z}^{21} & \mathcal{Z}^{22}\end{bmatrix}\begin{bmatrix} J^{\mathrm{v}}\\ J^{\varphi}\end{bmatrix}+\begin{bmatrix} \mathcal{X}^{11} & \mathcal{X}^{12}\\ \mathcal{X}^{21} & \mathcal{X}^{22}\end{bmatrix}\begin{bmatrix} M^{\mathrm{v}}\\ M^{\varphi}\end{bmatrix}=\begin{bmatrix} 0\\ 0\end{bmatrix}\tag{10}$$

Combining the matrix systems for the integral representation (9) and (10) gives, in short-hand notation,

$$\begin{bmatrix} Z & X\\ \mathcal{Z} & \mathcal{X}\end{bmatrix}\begin{bmatrix} J\\ M\end{bmatrix}=\begin{bmatrix} E\\ 0\end{bmatrix}$$

The magnitude of the entries of the matrices may differ by several orders of magnitude. To avoid numerical errors, the system is solved for one current at a time,

$$J=-\mathcal{Z}^{-1}\mathcal{X}M \implies \Big\{-Z\mathcal{Z}^{-1}\mathcal{X}+X\Big\}M=E\tag{11}$$

when $\mathbf{J}$ is eliminated. In the first line, $\mathbf{J}$ is expressed as a function of $\mathbf{M}$ utilizing the integral equation. The matrix $\mathcal{Z}$ is a square matrix and inverted numerically in MATLAB. The second equation is ill-posed. The matrix is no longer a square matrix and to solve for $\mathbf{M}$, the linear system is inverted and regularized by the singular value decomposition (SVD) in MATLAB [42]. Besides numerical errors also noise and measurement errors show up. Here, the SVD helps in suppressing the amplification of noise in the inversion [43]. The cut-off value, i.e., the magnitude of the largest singular value that is excluded, is proportional to the largest singular value of the largest Fourier component of the measured field. The proportionality constant is chosen as 0.1 and 0.3 when reconstructing the co- and the cross-component, respectively [43].

In our initial investigation we have not encountered any problems with spurious modes [44] or by using the numerical inversion of MATLAB or the SVD. However, a more detailed investigation of the ill-posed equations and the choice of the cut-off value, is planned to be addressed in a forthcoming paper.

3. NEAR-FIELD MEASUREMENTS

The experimental set-up and the measured electric field is described in [45]. However, for convenience, the necessary information is summarized. The measurement set-up is shown in Figure 3. A reflector antenna, fed by a symmetrically mounted wave-guide, generates the electromagnetic field. The diameter of the antenna is 0.32 m, and the main lobe of the antenna is vertically polarized relative to the horizontal plane. The radome surface is axially symmetric and its radius, in terms of the height coordinate, is modeled by

$$\rho(z) = \begin{cases} 0.213\,\mathrm{m} & -0.728\,\mathrm{m} \leq z \leq -0.663\,\mathrm{m} \\ -(bz' + d) + \sqrt{(bz' + d)^2 - a(z')^2 - 2cz' - e} & \\ & -0.663\,\mathrm{m} < z \leq 0.342\,\mathrm{m} \end{cases}$$

where $z' = z + 0.728\,\mathrm{m}$ and the constants are $a = 0.122$, $b = 0.048$, $c = -0.018\,\mathrm{m}$, $d = 0.148\,\mathrm{m}$, and $e = -0.108\,\mathrm{m}^2$, respectively. The height of the radome corresponds to 29 wavelengths for the frequency 8.0 GHz. The material of the radome has a relative permittivity of about 4.32 and its loss tangent is about 0.0144. The thickness of the wall of the radome varies over the surface in the interval 7.6–8.2 mm.

The surface S_{rad} in (5) and (8) is defined by the radome surface, closed with smooth top and bottom surfaces. These added surfaces are needed since the integral representation applies to a closed surface and the measurements are performed under non-ideal conditions. The turntable, on which the antenna and radome are located, see Figure 3(a), reflects some of the radiation, which is taken care of by the added bottom surface. The top surface takes care of the electric field that is reflected on the inside of the radome and then radiated through the top hole. If these factors are neglected, unwanted edge effects occur, since the electric fields originating from the turntable and the top of the radome are forced to originate from the radome itself. The radome surface is divided into 8 cells per wavelength in the height direction, and in each cell 4 points are chosen where the integrations are evaluated.

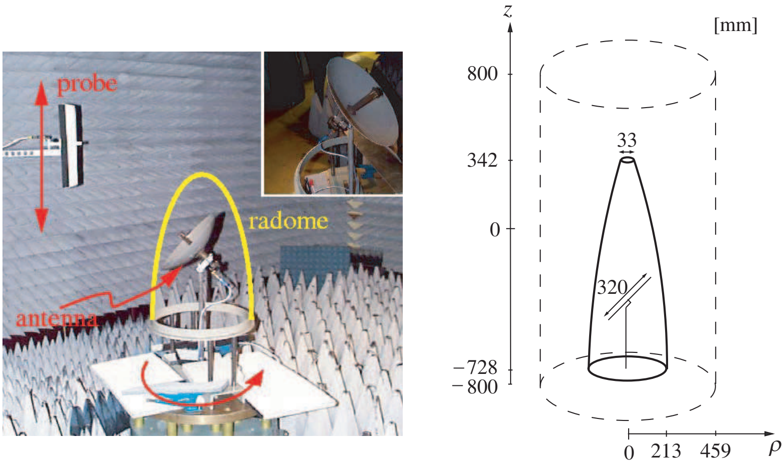

(a) (b)

Figure 3. (a) Photo of the cylindrical near-field range at SAAB Bofors Dynamics, Sweden. The antenna under test is rotated and the probe is moved in the vertical direction. A close up of the reflector antenna is shown in the upper right corner. (b) The dimensions of the reflector antenna, the radome, and the cylinder where the electric near field is measured.

The electric field is measured on a cylindrical surface by moving the probe in the z-direction and rotating the radome and the antenna under test, see Figure 3. This surface is located in the near-field zone [46]. The near-field measurement probe consists of an IEC R100 waveguide, with a collar of radar absorbing material, for which no compensation is made in the final data. The waveguide is linearly polarized, i.e., one polarization is measured after which the waveguide is turned 90 degrees. The accuracy of the turntable and the probe is 0.00025 degrees and 0.12 mm, respectively. For every movement of the probe, Δz, the turntable is rotated 360 degrees. With this measurement set-up, the data on the top and the bottom of the cylindrical surface cannot be collected. It would have been preferable to measure the fields on an infinite cylinder. However, the size of the cylinder is chosen such that the turntable below the radome does not have a major influence on the measurements and such that the fields above $z = 800$ mm are negligible. In the azimuth angle, 120 points are measured in steps of 3°. The z-dimension is divided into 129 points, every two points, v_q and v_{q+1}, are separated by 12.5 mm. The sample density fulfills the sampling theorem for cylindrical near-field measurements given in, e.g., [2].

Three different measurement configurations are considered; antenna without radome, antenna together with radome, and antenna together with defect radome. The defect radome has two copper plates attached to its surface. These are located in the forward direction where the main lobe hits the radome and centered at the heights 41.5 cm and 65.5 cm above the bottom of the radome. The side of the squared copper plates is 6 cm, corresponding to 1.6 wavelengths at 8.0 GHz. The absolute values of the measured co- and cross-polarized electric fields, E^{v} and E^{φ}, respectively, are shown in Figures 4 and 5, where $|E^{\mathrm{v}}|_{\mathrm{dB}} = 20\log(|E^{\mathrm{v}}|/|E^{\mathrm{v}}|_{\max})$

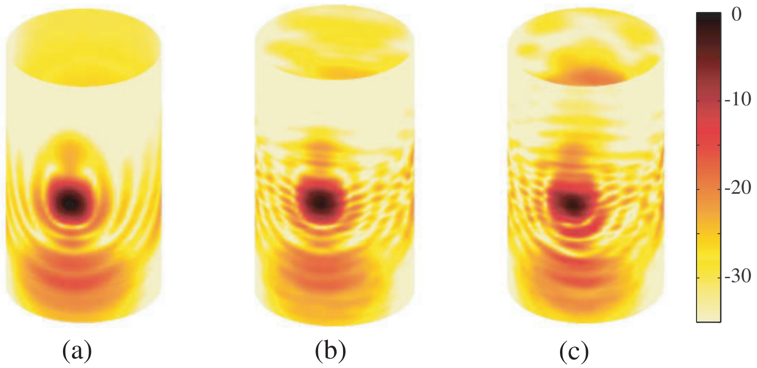

(a) (b) (c)

Figure 4. The co-component, $|E^{\mathrm{v}}|_{\mathrm{dB}}$, of the experimentally measured near-field data at 8.0 GHz, normalized with the largest value of $|E^{\mathrm{v}}|$ when no radome is present. (a) No radome present. (b) Radome present. (c) Defect radome present.

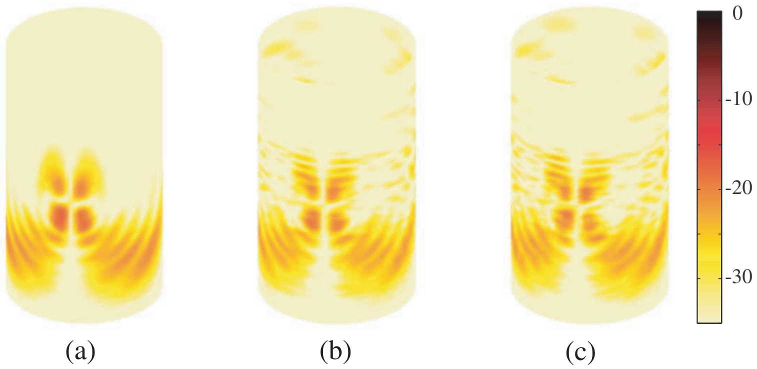

(a) (b) (c)

Figure 5. The cross-component, $|E^{\varphi}|_{\mathrm{dB}}$, of the experimentally measured near-field data at 8.0 GHz, normalized with the largest value of $|E^{\mathrm{v}}|$ when no radome is present. (a) No radome present. (b) Radome present. (c) Defect radome present.

and $|E^{\varphi}|_{\rm dB} = 20\log(|E^{\varphi}|/|E^{\rm v}|_{\max})$, respectively. That is, all fields are normalized with the largest value of $|E^{\rm v}|$ when no radome is present. In particular, E^{φ} has a quite complicated pattern. The diffraction is explained as environmental reflections and an off-centered antenna feed. Observe that the amplitude of the azimuth component is smaller than the amplitude of the height component, i.e., measurement errors are more likely to show up here. The differences between the three different antenna and radome cases arise from constructive and destructive interference between the radiated field and the scattered field. The absolute value of the Fourier transformed measured fields are shown in dB-scale in Figures 6 and 7. According to these figures, the spectrum is truncated at $n = 30$, above which the energy contents is too low.

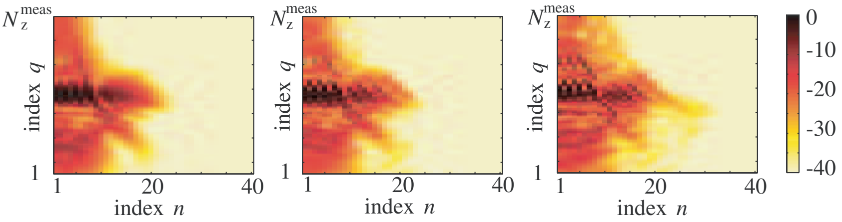

(a) (b) (c)

Figure 6. The Fourier transformed measured field, $|E^{\rm v}|_{\rm dB}$, at 8.0 GHz. All values are normalized with the largest value of $|E^{\rm v}|$ when no radome is present. (a) No radome present. (b) Radome present. (c) Defect radome present.

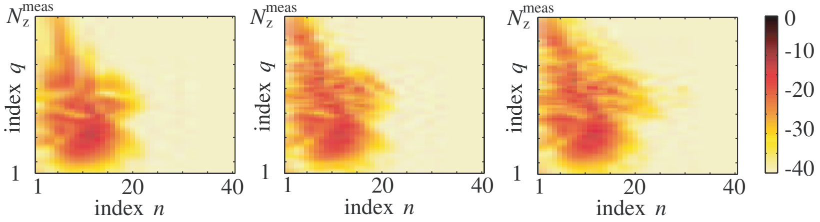

(a) (b) (c)

Figure 7. The Fourier transformed measured field, $|E^{\varphi}|_{\rm dB}$, at 8.0 GHz. All values are normalized with the largest value of $|E^{\rm v}|$ when no radome is present. (a) No radome present. (b) Radome present. (c) Defect radome present.

4. RESULTS

The measured field on the cylindrical surface at 8.0 GHz, cf., Figures 4 and 5, is transformed back onto a surface corresponding to the radome surface. Figures 8 and 9 show the recreated electric fields, $|E^{\mathrm{v}}|_{\mathrm{dB}}$ and $|E^{\varphi}|_{\mathrm{dB}}$, respectively, in the main lobe for the different configurations. Observe that all values are normalized with the largest value of $|E^{\mathrm{v}}|$ when the defect radome is present. The figures show that the near field close to the antenna is complex and hard to predict. In the case, when no radome is located around the antenna, the electric fields are calculated on a surface shaped as the radome, see Figures 8(a) and 9(a). The case when the radome is present, see Figures 8(b) and 9(b), shows that the radome interacts with the antenna and hence disturbs the radiated field. How this interaction affects the amplitude is depicted in Figures 10(a) and (b), where $(|E^{\mathrm{v}}_{\text{no radome}}| - |E^{\mathrm{v}}_{\text{radome}}|)$ and $(|E^{\varphi}_{\text{no radome}}| - |E^{\varphi}_{\text{radome}}|)$ are shown in a linear scale and normalized with the maximum difference for each component. Both components of the electric field are reduced in amplitude in the main lobe whereas the field strength outside the main lobe is increased when the radome is introduced. This is most likely due to transmission loss in the radome wall and scattering against the inside wall.

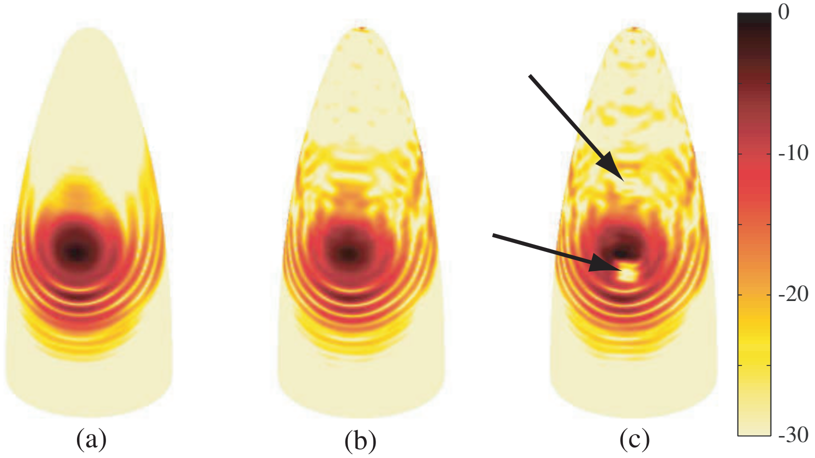

(a) (b) (c)

Figure 8. The recreated $|E^{\mathrm{v}}|_{\mathrm{dB}}$-component on the front side of the radome. All values are normalized with the largest value of $|E^{\mathrm{v}}|$ when the defect radome is present. (a) No radome present. (b) Radome present. (c) Defect radome present. The arrows point out the locations of the copper plates.

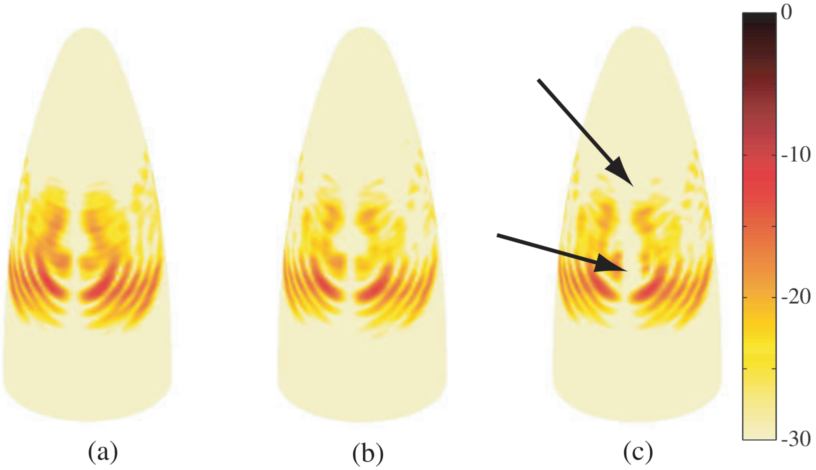

(a) (b) (c)

Figure 9. The recreated $|E^{\varphi}|_{\mathrm{dB}}$-component on the front side of the radome. All values are normalized with the largest value of $|E^{\mathrm{v}}|$ when the defect radome is present. (a) No radome present. (b) Radome present. (c) Defect radome present. The arrows point out the locations of the copper plates.

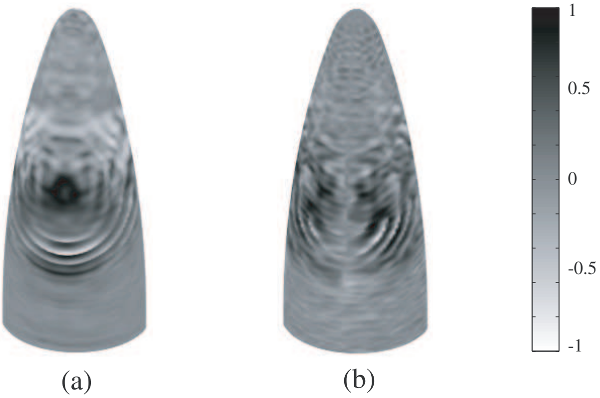

(a) (b)

Figure 10. The subtraction between the fields with and without radome present on the front side of the radome. In (a) $(|E^{\mathrm{v}}_{\text{no radome}}| - |E^{\mathrm{v}}_{\text{radome}}|)/\max||E^{\mathrm{v}}_{\text{no radome}}| - |E^{\mathrm{v}}_{\text{radome}}||$ is shown and in (b) $(|E^{\varphi}_{\text{no radome}}| - |E^{\varphi}_{\text{radome}}|)/\max||E^{\varphi}_{\text{no radome}}| - |E^{\varphi}_{\text{radome}}||$. The scale is linear.

The effect of the attached copper plates are detected as shown in Figures 8(c) and 9(c), where the lower plate appears clearly. Observe that the copper plates cannot be localized directly in the near-field data, compare Figures 4(c) and 5(c) to Figures 8(c) and 9(c). The near-field data only shows that the field is disturbed, not the locations of the disturbances. The upper plate is hard to discern in Figures 8(c) and 9(c), since it is located in a region with small field magnitudes. However, the influence of the upper copper plate can be detected in the cross section graphs, see Figures 11(a) and (b). To determine the exact position of the defects several cross section graphs have to be examined. It is interesting to see that even though the magnitude of the cross-polarization is small, the locations of the copper plates can be found.

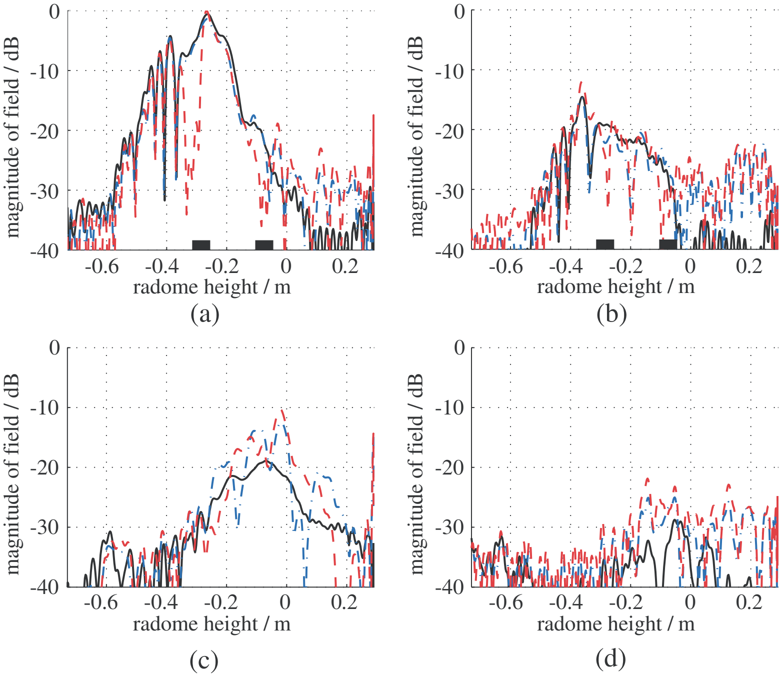

(a) (b)

(c) (d)

Figure 11. Cross sections of the reconstructed field components. (a) $|E^{\mathrm{v}}|_{\mathrm{dB}}$ in the main lobe. (b) $|E^{\varphi}|_{\mathrm{dB}}$ in the main lobe. (c) $|E^{\mathrm{v}}|_{\mathrm{dB}}$ on the back of the radome. (d) $|E^{\varphi}|_{\mathrm{dB}}$ on the back of the radome. All values are normalized with the maximum value of $|E^{\mathrm{v}}|$ when the defect radome is present. The solid black line corresponds to no radome, the dashed dot blue line has the radome present and the dashed red line represents the defect radome. The positions of the copper plates on the defect radome are marked by thick lines on the horizontal axis.

The presence of the radome also creates some backscattering (flash lobes) as seen in Figures 11(c), 11(d), 12, and 13. In Figures 11(c) and 11(d), a cross section at an angle 180° from the center of the main lobe, i.e., in the middle of the back side, is viewed. Figures 12 and 13 depict both components on the back side of the radome for all three configurations in a dB-scale. In these figures it is also observed that the flash lobes are altered when the copper plates are present.

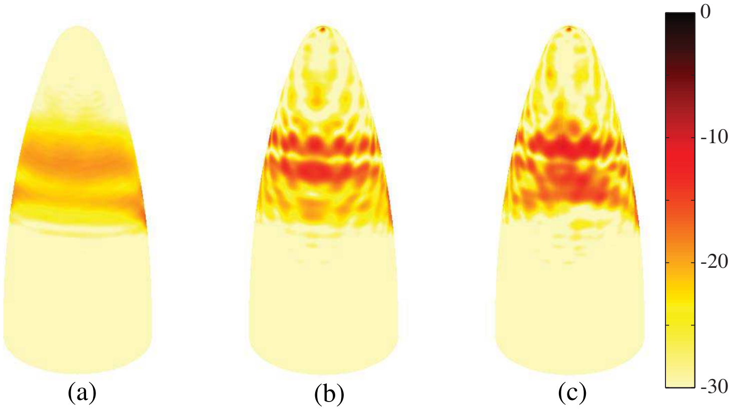

Figure 12. The recreated $|E^{\mathrm{v}}|_{\mathrm{dB}}$-component on the back side of the radome. All values are normalized with the maximum value of $|E^{\mathrm{v}}|$, on the front side, when the defect radome is present. (a) No radome present. (b) Radome present. (c) Defect radome present.

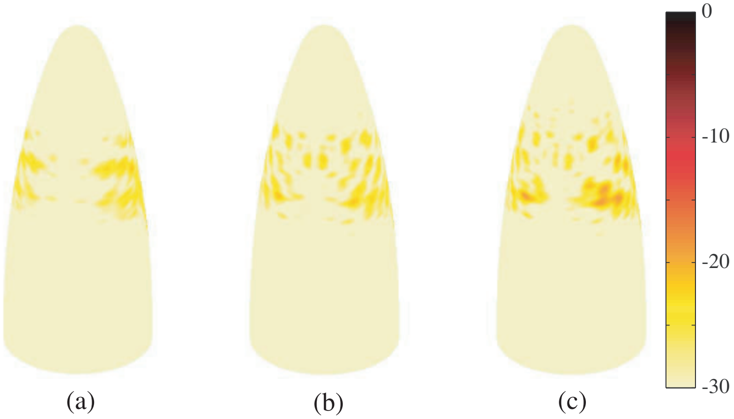

Figure 13. The recreated $|E^{\varphi}|_{\mathrm{dB}}$-component on the back side of the radome. All values are normalized with the maximum value of $|E^{\mathrm{v}}|$, on the front side, when the defect radome is present. (a) No radome present. (b) Radome present. (c) Defect radome present.

The copper plates can also be detected by subtracting the field of the defect radome and the field of the non-defect radome. This result is shown in dB-scale in Figure 14 for both the components of the electric field, i.e., $|E^{\mathrm{v}}_{\mathrm{radome}} - E^{\mathrm{v}}_{\mathrm{def\ radome}}|_{\mathrm{dB}}$ and $|E^{\varphi}_{\mathrm{radome}} - E^{\varphi}_{\mathrm{def\ radome}}|_{\mathrm{dB}}$, each component normalized with the maximum difference for each component. The reconstruction of the E^{φ}-component, cf., Figure 14(b), only shows the effects of some parts of the copper plates. The reason is that parts of the copper plates are located in an area where the amplitude of the E^{φ}-component is small, cf., Figures 5 and 9(a).

Figure 14(a) indicates that there is an amplitude difference between the configurations slightly above the location of the lower copper plate. To visualize what is happening, the difference $(|E^{\mathrm{v}}_{\mathrm{radome}}| - |E^{\mathrm{v}}_{\mathrm{def\ radome}}|)$, normalized with its maximum value, in a linear scale, is depicted in Figure 15. The scale is truncated in order to see the small field difference above the copper plate. Here it becomes clear that the area, where the copper plate is attached, has a reduced electric field, when the defect radome is present. The area above the copper plate has instead an increased electric field, when the defect radome is present. This is most likely due to scattering of the copper plate.

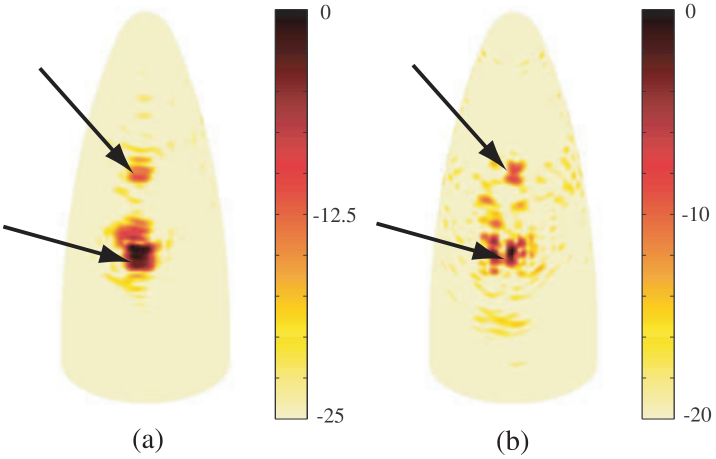

(a) (b)

Figure 14. The logarithmic differences revealing the copper plates, (a) $20\log\{|E^{\mathrm{v}}_{\mathrm{radome}} - E^{\mathrm{v}}_{\mathrm{def\ radome}}|/\max|E^{\mathrm{v}}_{\mathrm{radome}} - E^{\mathrm{v}}_{\mathrm{def\ radome}}|\}$, and (b) $20\log\{|E^{\varphi}_{\mathrm{radome}} - E^{\varphi}_{\mathrm{def\ radome}}|/\max|E^{\varphi}_{\mathrm{radome}} - E^{\varphi}_{\mathrm{def\ radome}}|\}$ on the front side of the radome. The arrows point out the locations of the copper plates.

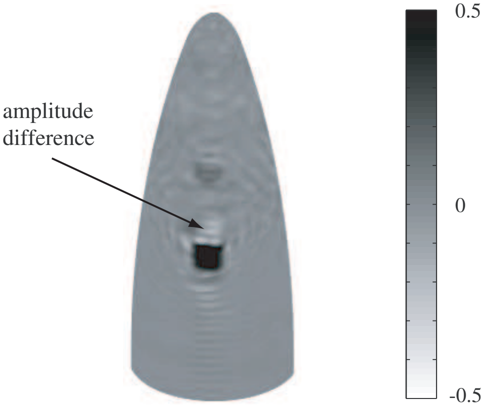

Figure 15. The difference $(|E^{\mathrm{v}}_{\mathrm{radome}}| - |E^{\mathrm{v}}_{\mathrm{def\ radome}}|)/\max||E^{\mathrm{v}}_{\mathrm{radome}}| - |E^{\mathrm{v}}_{\mathrm{def\ radome}}||$ in a linear scale on the front side of the radome. The scale is truncated in order to see the small field amplitude above the copper plate, marked with an arrow.

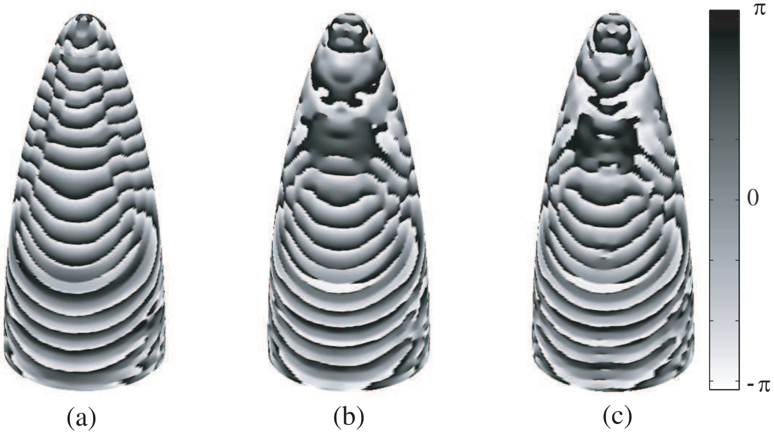

Figure 16. The recreated phase of the E^{v}-component on the front side of the radome in a linear scale. (a) No radome present. (b) Radome present. (c) Defect radome present.

So far only the amplitudes of the reconstructed fields has been investigated. However, even the phase can give useful information. The phase of the E^{v}-component, i.e., $\angle E^{\mathrm{v}}$, where $\angle$ denotes the argument, is depicted in Figure 16 for all configurations. The vertical lines above the main lobe in Figure 16(a) are due to phase jumps, and are caused by the low amplitude of the fields in these areas.

Just showing the phase as in Figure 16 does not give very much information. What is interesting is to study the phase difference (antenna — antenna with radome) for the two recreated components, see Figure 17. It reveals how the phase is changed due to the influence of the radome. It is observed that the phase shift in the main lobe is almost constant, for both components. This confirms that the radome is well adapted to the frequency 8.0 GHz. Since the amplitude of E^{φ} is low, cf., Figures 5 and 9, its phase contains much noise, and it is therefore somewhat more unreliable than $\angle E^{\mathrm{v}}$.

In Figure 18, a cross section in the middle of the main lobe of the phase difference in Figure 17 is depicted. The cross section of $\angle E^{\varphi}$ is shown for a slightly acentric angle, since the amplitude in the center of the main lobe is very low, see Figure 9. In areas where the field is strong, the phase shift does not fluctuate as much. Outside this areas the amplitude is low and the phase is not well defined, i.e., dominated by noise, and it will not give valid information. This means that when looking at the main lobe, the only area that contains reliable values is $z \in [-0.5, -0.05]$.

The phase shift arising when the radome is introduced, i.e., the phase shift viewed in Figures 17 and 18, is called the IPD (Insertion Phase Delay). It is one of the parameters that quantifies the performance of the radome, and depending on the polarization, two different IPD are defined [47]

$$T = |T|\angle \mathrm{IPD} \tag{12}$$

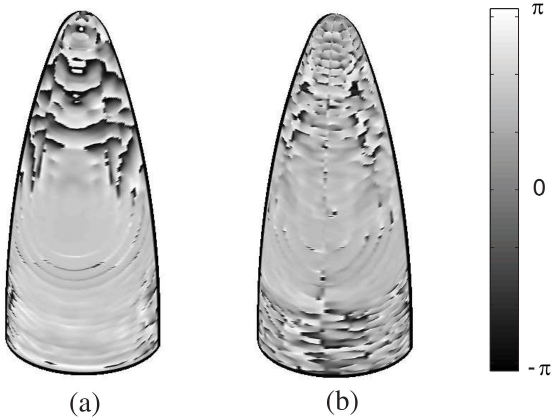

(a) (b)

Figure 17. The IPD, i.e., the phase difference between the field when no radome is present and the field when the radome is present, on the front side of the radome. (a) $(\angle E^{\mathrm{v}}_{\text{no radome}} - \angle E^{\mathrm{v}}_{\text{radome}})$. (b) $(\angle E^{\varphi}_{\text{no radome}} - \angle E^{\varphi}_{\text{radome}})$.

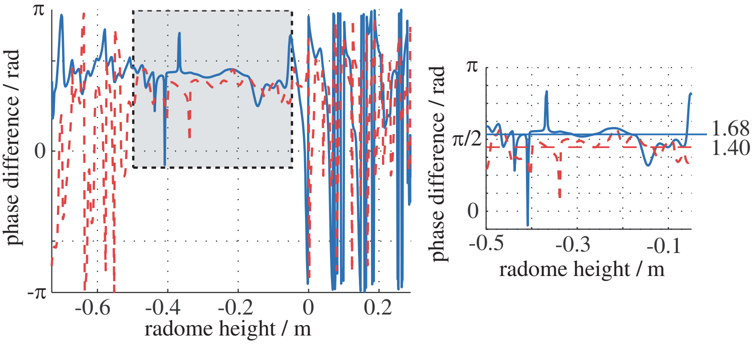

Figure 18. Cross section in the middle of the main lobe of the IPD depicted in Figure 17. The solid blue line corresponds to $(\angle E^{\mathrm{v}}_{\text{no radome}} - \angle E^{\mathrm{v}}_{\text{radome}})$ and the dashed red to $(\angle E^{\varphi}_{\text{no radome}} - \angle E^{\varphi}_{\text{radome}})$, respectively. The insert shows the area with reliable data and the medians.

where $T = E_{\mathrm{t}}/E_{\mathrm{i}}$ is the complex transmission coefficient. The incoming field is denoted E_{i}, and the transmitted E_{t}. The phase shift is only known modulus 2π. To validate the calculation of the IPD, an estimation of the thickness of the radome wall is carried out. Under the assumption of negligible reflections the IPD can be expressed as [48]

$$\mathrm{IPD} = \frac{\omega}{\mathrm{c}}\left\{\mathrm{Re}\sqrt{\epsilon_{\mathrm{r}}(1 - \mathrm{j}\tan\delta)}\cos\theta_{\mathrm{t}} - \cos\theta_{\mathrm{i}}\right\}d \tag{13}$$

for both polarizations, where ω is the angular frequency, c is the speed of light in vacuum, θ_{i} is the incident angle, and θ_{t} is the transmission angle of the field on the inside of the radome wall. Approximate values of the relative permittivity, $\epsilon_{\mathrm{r}} \approx 4.32$, and the loss tangent, $\tan\delta \approx 0.0144$, are used. The thickness of the radome wall is denoted d. The incident angle is approximated to 40°, cf., Figure 3(b). The measured radome thickness, d, varies over the surface in the interval 7.6–8.2 mm. The phase shift in the main lobe is taken as the medians of the calculated IPD, see the insert in Figure 18. The medians, for $z \in [-0.5, -0.05]$, are 1.68 rad and 1.40 rad for the co- and the cross-component, respectively. Solving for d in (13) results in a radome thickness of 6.9–8.3 mm. The agreement is quite well considering the approximations made.

An investigation of the phase difference (radome-defect radome), see Figures 19 and 20, reveals that its harder to localize the actual positions of the copper plates by using the phase instead of only the amplitude, cf., Figures 8 and 9. Nevertheless, the upper copper plate is visible in the 3-D visualization in Figure 19(a), and by looking at a cross section over the main lobe of the phase difference, the position of

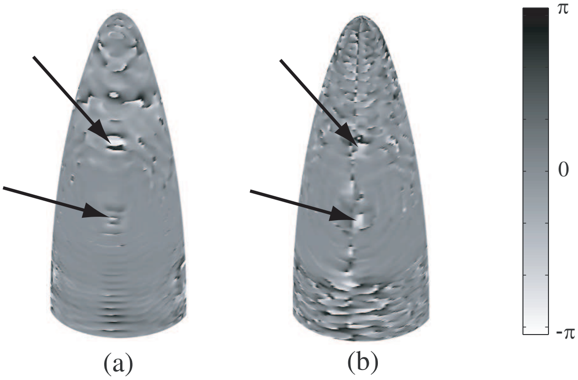

(a) (b)

Figure 19. The phase difference between the field when the radome is present and the field when the defect radome is present, on the front side of the radome. The arrows point out the copper plates. (a) $(\angle E^{\mathrm{v}}_{\mathrm{radome}} - \angle E^{\mathrm{v}}_{\mathrm{def\ radome}})$. (b) $(\angle E^{\varphi}_{\mathrm{radome}} - \angle E^{\varphi}_{\mathrm{def\ radome}})$.

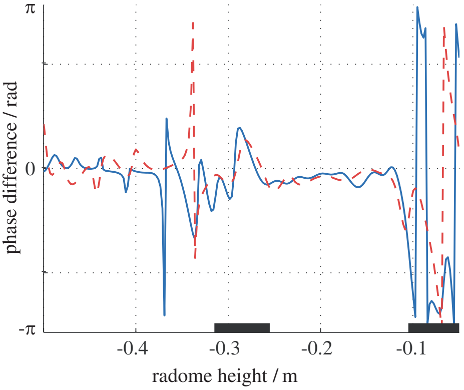

Figure 20. Cross section in the middle of the main lobe of the phase differences depicted in Figure 19. The axis describing the radome height is truncated and shows only the region where the phase information is reliable, cf., Figure 18. The blue solid line corresponds to $(\angle E^{\mathrm{v}}_{\mathrm{radome}} - \angle E^{\mathrm{v}}_{\mathrm{def\ radome}})$ and the red dashed to $(\angle E^{\varphi}_{\mathrm{radome}} - \angle E^{\varphi}_{\mathrm{no\ radome}})$, respectively.

the upper copper plate is located for both components, see Figure 20. We only show the interval, where the phase is not too contaminated by noise, cf., Figure 18. The upper copper plate is located on the boundary to where noise dominates. Thus, if the positions of the copper plate were not known in advance, the phase shift might be interpreted as noise. The lower copper plate also introduces a phase shift, but these effects are hard to interpret and not confined to the exact position of the plate.

5. CONCLUSION

The aim of this paper is to reconstruct equivalent currents on a surface bounding the sources of an electromagnetic field. A vector-valued surface integral representation is utilized together with the extinction theorem. The surface integral representation gives a linear map between the equivalent surface currents and the near-field data for general geometries. It is shown that this map can be inverted for axially symmetric geometries with the measured near field. The theory can be adapted to geometries lacking symmetry axes. However, it is not a feasible approach for radome applications today due to the computational demand to solve the integral equations. An alternative approach would be to address this problem using fast multipoles methods [49].

In previous papers only the dominating vertical co-component of the measured field has been used in the reconstruction by using a scalar integral representation, where comparison with measured far field shows good agreement [45, 50]. In this paper it is shown that both components of the equivalent currents can be reconstructed by using a full-wave surface integral representation. The results for the cross-component show that also this component provides useful insight of the complex field close to the antenna and the field altered by the radome. It is illustrated how the radome interacts with the electric field. In particular, transmission losses in the radome wall and reflections on the inside decrease the field in the main lobe, and new side and flash lobes appear. Both components of the experimentally measured field can also be used to locate the effect of defects, i.e., copper plates, not directly visible in the measured near-field data. Furthermore, the copper plates introduce scattering and alter the flash lobes.

Also, the phase of the reconstructed fields is investigated. The IPD, i.e., the phase difference, arising when the radome is located between the antenna and the measurement probe, is visualized. The results give a good estimate of the thickness of the radome wall. The effects of the copper plates are visible in the phase shift. However, the exact location of the defects is hard to determine solely from the phase images.

This paper shows the potentials of the approach in radome diagnostics. Next step is to analyze if the electric equivalent current, i.e., the magnetic field, on the radome surface gives some more information. Moreover, investigations with different frequencies are expected. To localize the exact positions of the defects, a deeper analyze of 3D-pictures, cf., Figures 8(c) and 9(c), and cross-section graphs, cf., Figure 11, combined with the phase shift data, is planned. To use this method in verifying radomes, i.e., calculating the IPD, more analysis of the phase and its noise levels is planned to be addressed in a forthcoming paper.

ACKNOWLEDGMENT

The work reported in this paper was made possible by a grant from the Swedish Defense Material Administration, and their support is gratefully acknowledged. We are indebted to Saab Bofors Dynamics, in particular Ola Forslund for assistance on measurement details, and Applied Composites AB, for providing measurement data. In discussing the concepts of IPD, Michael Andersson has been most helpful, and his assistance is most appreciated.

REFERENCES

1. Hansen, J. E. (ed.), *Spherical Near-Field Antenna Measurements*, *IEE Electromagnetic Waves Series*, No. 26, Peter Peregrinus Ltd., Stevenage, UK, 1988.
2. Yaghjian, A. D., "An overview of near-field antenna measurements," *IEEE Trans. Antennas Propagat.*, Vol. 34, No. 1, 30–45, January 1986.
3. Rahmat-Samii, Y., L. I. Williams, and R. G. Yaccarino, "The UCLA bi-polar planar-near-field antenna-measurement and diagnostics range," *IEEE Antennas and Propagation Magazine*, Vol. 37, No. 6, 16–35, December 1995.
4. Shifflett, J. A., "CADDRAD: A physical optics radar/radome analysis code for arbitrary 3D geometries," *IEEE Antennas and Propagation Magazine*, Vol. 6, No. 39, 73–79, 1997.
5. Andersson, M., "Software for analysis of radome performance," *Proc. International Conference on Electromagnetics in Advanced Applications (ICEAA'05)*, 537–539, Torino, Italy, 2005.
6. Lee, J., E. M. Ferren, D. P. Woollen, and K. M. Lee, "Near-field probe used as a diagnostic tool to locate defective elements in an array antenna," *IEEE Trans. Antennas Propagat.*, Vol. 36, No. 6, 884–889, 1988.
7. Rochblatt, D. J. and B. L. Seidel, "Microwave antenna holography," *IEEE Trans. Microwave Theory Tech.*, Vol. 40, No. 6, 1294–1300, 1992.

8. Corey, L. E. and E. B. Joy, "On computation of electromagnetic fields on planar surfaces from fields specified on nearby surfaces," *IEEE Trans. Antennas Propagat.*, Vol. 29, No. 2, 402–404, 1981.
9. Fridén, J., H. Isaksson, B. Hansson, and B. Thors. "Robust phase-retrieval for quick whole-body SAR assessment using dual plane amplitude-only data," *Electronics Letters*, Vol. 45, No. 23, 1155–1157, 2009.
10. Marengo, E. A. and A. J. Devaney, "The inverse source problem of electromagnetics: Linear inversion formulation and minimum energy solution," *IEEE Trans. Antennas Propagat.*, Vol. 47, No. 2, 410–412, Feb. 1999.
11. Nordebo, S., M. Gustafsson, and K. Persson, "Sensitivity analysis for antenna near-field imaging," *IEEE Trans. Signal Process.*, Vol. 55, No. 1, 94–101, Jan. 2007.
12. Guler, M. G. and E. B. Joy, "High resolution spherical microwave holography," *IEEE Trans. Antennas Propagat.*, Vol. 43, No. 5, 464–472, 1995.
13. Sten, J. C.-E. and E. A. Marengo, "Inverse source problem in the spheroidal geometry: Vector formulation," *IEEE Trans. Antennas Propagat.*, Vol. 56, No. 4, 961–969, 2008.
14. Cappellin, C., O. Breinbjerg, and A. Frandsen, "Properties of the transformation from the spherical wave expansion to the plane wave expansion," *Radio Sci.*, Vol. 43, No. 1, RS1012, 2008.
15. Cappellin, C., A. Frandsen, and O. Breinbjerg, "Application of the SWE-to-PWE antenna diagnostics technique to an offset reflector antenna," *IEEE Antennas and Propagation Magazine*, Vol. 50, No. 5, 204–213, 2008.
16. Ziyyat, A., L. Casavola, D. Picard, and J. C. Bolomey, "Prediction of BTS antennas safety perimeter from NF to NF transformation: An experimental validation," *Proc. Antenna Measurement Techniques Association (AMTA)*, 22–26, Denver, US, 2001.
17. Soldovieri, F., C. Mola, R. Solimene, and R. Pierri. "Inverse source problem from the knowledge of radiated field over multiple rectilinear domains," *Progress In Electromagnetics Research M*, Vol. 8, 131–141, 2009.
18. Thérond, F., J. C. Bolomey, N. Joachmowicz, and F. Lucas, "Electromagnetic diagnosis technique using spherical near-field probing," *Proc. EUROEM'94*, 1218–1226, Bordeaux, France, 1994.
19. Peterson, A. F., S. L. Ray, and R. Mittra, *Computational Methods*

for Electromagnetics, IEEE Press, New York, 1998.

20. Shore, R. A. and A. D. Yaghjian, "Dual surface electric field integral equation," Air Force Research Laboratory Report, 2001.
21. Sarkar, T. K. and A. Taaghol, "Near-field to near/far-field transformation for arbitrary near-field geometry utilizing an equivalent electric current and MoM," *IEEE Trans. Antennas Propagat.*, Vol. 47, No. 3, 566–573, Mar. 1999.
22. Laurin, J.-J., J.-F. Zürcher, and F. E. Gardiol, "Near-field diagnostics of small printed antennas using the equivalent magnetic current approach," *IEEE Trans. Antennas Propagat.*, Vol. 49, No. 5, 814–828, 2001.
23. Las-Heras, F., M. R. Pino, S. Loredo, Y. Alvarez, and T. K. Sarkar, "Evaluating near-field radiation patterns of commercial antennas," *IEEE Trans. Antennas Propagat.*, Vol. 54, No. 8, 2198–2207, 2006.
24. Las-Heras, F., B. Galocha, and Y. Alvarez, "On the sources reconstruction method application for array and aperture antennas diagnostics," *Microwave Opt. Techn. Lett.*, Vol. 51, No. 7, 1664–1668, 2009.
25. Eibert, T. F. and C. H. Schmidt, "Multilevel fast multipole accelerated inverse equivalent current method employing Rao-Wilton-Glisson discretization of electric and magnetic surface currents," *IEEE Trans. Antennas Propagat.*, Vol. 57, No. 4, 1178–1185, 2009.
26. Quijano, J. L. A. and G. Vecchi, "Improved-accuracy source reconstruction on arbitrary 3-D surfaces," *IEEE Antennas & Wireless Propagat. Lett.*, Vol. 8, 1046–1049, 2009.
27. Colton, D. and R. Kress, *Integral Equation Methods in Scattering Theory*, John Wiley & Sons, New York, 1983.
28. Ström, S., "Introduction to integral representations and integral equations for time-harmonic acoustic, electromagnetic and elastodynamic wave fields," *Field Representations and Introduction to Scattering*, *Handbook on Acoustic, Electromagnetic and Elastic Wave Scattering*, V. V. Varadan, A. Lakhtakia, and V. K. Varadan (eds.), Vol. 1, Ch. 2, 37–141, Elsevier Science Publishers, Amsterdam, 1991.
29. Persson, K., M. Gustafsson, and G. Kristensson, "Reconstruction and visualization of equivalent currents on a radome using an integral representation formulation," Technical Report LUTEDX/(TEAT-7184)/1–45/(2010), Lund University, Department of Electrical and Information Technology, P. O. Box 118, S-221 00 Lund, Sweden, 2010, http://www.eit.lth.se.

30. Silver, S., *Microwave Antenna Theory and Design*, *Radiation Laboratory Series*, Vol. 12, McGraw-Hill, New York, 1949.
31. Kleinman, R. E. and G. F. Roach, "Boundary integral equations for the three-dimensional Helmholtz equation," *SIAM Review*, Vol. 16, No. 2, 214–236, 1974.
32. Müller, C., *Foundations of the Mathematical Theory of Electromagnetic Waves*, Springer-Verlag, Berlin, 1969.
33. Jones, D. S., *Acoustic and Electromagnetic Waves*, Oxford University Press, New York, 1986.
34. Nieto-Vesperinas, M., *Scattering and Diffraction in Physical Optics*, 2nd edition, World Scientific Publisher, Singapore, 2006.
35. Balanis, C. A., *Advanced Engineering Electromagnetics*, John Wiley & Sons, New York, 1989.
36. Morita, N., N. Kumagai, and J. R. Mautz, *Integral Equation Methods for Electromagnetics*, Artech House, Boston, London, 1990.
37. Poggio, A. J. and E. K. Miller, "Integral equation solutions of three-dimensional scattering problems," *Computer Techniques for Electromagnetics*, R. Mittra (ed.), Pergamon, New York, 1973.
38. Bondeson, A., T. Rylander, and P. Ingelström, *Computational Electromagnetics*, Springer-Verlag, Berlin, 2005.
39. Kress, R., *Linear Integral Equations*, 2nd edition, Springer-Verlag, Berlin Heidelberg, 1999.
40. Mautz, J. R. and R. F. Harrington, "Radiation and scattering from bodies of revolution," *Appl. Scientific Research*, Vol. 20, No. 1, 405–435, 1969.
41. Andreasen, M., "Scattering from bodies of revolution," *IEEE Trans. Antennas Propagat.*, Vol. 13, No. 2, 303–310, 1965.
42. Strang, G., *Introduction to Applied Mathematics*, Wellesley-Cambridge Press, Box 157, Wellesley, MA 02181, 1986.
43. Aster, R., B. Borchers, and C. Thurber, *Parameter Estimation and Inverse Problems*, Academic Press, New York, 2005.
44. Shore, R. A. and A. D. Yaghjian, "Dual-surface integral equations in electromagnetic scattering," *IEEE Trans. Antennas Propagat.*, Vol. 53, No. 5, 1706–1709, 2005.
45. Persson, K. and M. Gustafsson, "Reconstruction of equivalent currents using a near-field data transformation — with radome applications," *Progress In Electromagnetics Research*, PIER 54, 179–198, 2005.
46. Balanis, C. A., *Antenna Theory*, 2nd edition, John Wiley & Sons, New York, 1997.

47. Kozakoff, D. J., *Analysis of Radome-enclosed Antennas*, Artech House, Boston, London, 1997.
48. Kong, J. A., *Electromagnetic Wave Theory*, John Wiley & Sons, New York, 1986.
49. Song, J. and W. Chew, "FMM and MLFMA in 3-D and fast Illinois solver code," *Fast and Efficient Algorithms in Computational Electromagnetics*, W. Chew, J.-M. Jin, E. Michielssen, and J. Song (eds.), 77–118, Artech House, 2001.
50. Persson, K. and M. Gustafsson, "Reconstruction of equivalent currents using the scalar surface integral representation," Technical Report LUTEDX/(TEAT-7131)/1–25/(2005), Lund University, Department of Electrical and Information Technology, P. O. Box 118, S-221 00 Lund, Sweden, 2005, http://www.eit.lth.se.